International Journal of Applied Earth Observations and Geoinformation 106 (2022) 102647

Contents lists available at ScienceDirect

International Journal of Applied Earth Observations and Geoinformation

journal homepage: www.elsevier.com/locate/jag

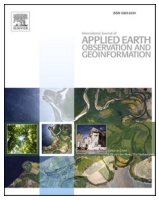

Surface meltwater runoff routing through a coupled supraglacial-proglacial drainage system, Inglefield Land, northwest Greenland

Ya Li [a,b], Kang Yang [a,b,c,*], Shuai Gao [a,b], Laurence C. Smith [d,e], Xavier Fettweis [f], Manchun Li [a,b]

[a] School of Geography and Ocean Science, Nanjing University, Nanjing, China
[b] Frontiers Science Center for Critical Earth Material Cycling, Nanjing University, Nanjing, China
[c] Southern Marine Science and Engineering Guangdong Laboratory, Zhuhai, China
[d] Institute at Brown for Environment and Society, Brown University, Providence, RI, USA
[e] Department of Earth, Environmental, and Planetary Sciences, Brown University, Providence, RI, USA
[f] Department of Geography, University of Liège, Liège, Belgium

ARTICLE INFO

Keywords:
Supraglacial river
Proglacial river
Surface mass balance
Sentinel-2
Greenland runoff

ABSTRACT

The northwest Greenland Ice Sheet (NW GrIS) is rapidly losing mass, and its ablation zone has expanded over the past two decades. Numerous supraglacial streams flowing directly over the NW GrIS surface drain a large lobe of grounded ice at Inglefield Land, into the proglacial Minturn River and the Nares Strait. Owing to the absence of moulins and crevasses, this continuous supraglacial-proglacial drainage system regulates the evacuation of surface meltwater from the ice sheet to the ocean. We examine this Inglefield Land coupled supraglacial-proglacial drainage system during the 2016–2019 melt seasons (July to August), using 137 Sentinel-2 and Landsat-8 visible/near-infrared satellite images. Two surface water metrics (supraglacial meltwater area fraction A_m and proglacial river effective width W_e) are used to track spatio-temporal variations of surface meltwater moving through this drainage system. Satellite-derived A_m and W_e are also compared with daily surface runoff simulations from the MAR v3.11 and MERRA-2 climate/SMB models, to estimate meltwater routing lag times and assess model performance. Satellite-derived A_m and W_e are highly correlated ($r^2 = 0.85$, $p < 0.01$), indicating that the coupled supraglacial-proglacial drainage system evacuates meltwater directly from the ice surface to the ocean with negligible subglacial storage or delays. Both remotely sensed metrics are positively correlated with modeled runoff, especially MAR ($r^2 = 0.81$ and 0.77 for A_m and W_e, vs. 0.66 and 0.64 for MERRA-2). Lagged MAR runoff (2 days, $r^2 = 0.87$ and 0.82) match both metrics better than simultaneous MAR runoff and the optimal time lag for both metrics are 2 d. We conclude that 1) unlike the southwest GrIS, the coupled supraglacial-proglacial drainage system at Inglefield Land routes surface meltwater runoff directly off the ice surface to the proglacial zone, with virtually no subglacial capture of runoff by moulins; 2) most of the ~2 d transit time occurs on the ice surface rather than in the proglacial zone; and 3) multi-temporal satellite imaging facilitates holistic, source-to-sink tracking of NW GrIS meltwater from the ice surface to the global ocean.

1. Introduction

The northwest Greenland Ice Sheet (NW GrIS) has experienced accelerating mass loss in the last two decades, making it one of the largest contributors to overall GrIS mass loss (Mouginot et al., 2019). Its ablation zone expanded twice as fast as the better-studied, intensely melting southwest (SW) GrIS from 1990 to 2017 (Noël et al., 2019). Surface meltwater runoff is the primary cause of NW GrIS mass loss (Ettema et al., 2009; Enderlin et al., 2014; Smith et al., 2017; Trusel et al., 2018) and is commonly estimated using climate models having explicit representation of ice sheet Surface Mass Balance (SMB) processes (Mankoff et al., 2020; Pitcher et al., 2020).

Climate/SMB models have two significant limitations when used to estimate surface meltwater runoff. First, runoff is computed as a residual of other SMB variables (Melt + Rainfall + Condensation – Refreezing – Retention) and thereby accumulates large uncertainties propagated from each variable (van den Broeke et al., 2009; Vernon et al., 2013; Smith et al., 2017; Lenaerts et al., 2019; Fettweis et al., 2020). Second, climate/SMB models ignore meltwater routing through supraglacial streams and rivers on the ice surface and thereby fail to replicate the

* Corresponding author at: School of Geography and Ocean Science, Nanjing University, Nanjing, China.
E-mail address: yangkangnju@gmail.com (K. Yang).

https://doi.org/10.1016/j.jag.2021.102647
Received 6 June 2021; Received in revised form 11 November 2021; Accepted 7 December 2021
Available online 17 December 2021

timing and magnitude of lateral runoff transport, especially at short (i.e. hours to days) time scales (Smith et al., 2017; van As et al., 2017). To incorporate this process, flow routing at an hourly to daily time scale should be observed and quantified.

Remote sensing techniques provide a direct investigation of the GrIS meltwater routing process. For example, Smith et al. (2015) mapped 523 supraglacial river networks on the SW GrIS from WorldView-1/2 images and found they create a highly efficient ice surface drainage system. Yang et al. (2021) studied dynamic supraglacial river networks and lakes on the SW GrIS with Landsat-8 images, and found that supraglacial lakes dominate instantaneous meltwater storage whereas supraglacial rivers dominate meltwater area. Overeem et al. (2015) compared changing inundation areas along the proglacial Watson River derived from MODIS images with simulated runoff from the RACMO regional climate model, and found considerable water storage within the ice sheet. However, most previous studies have focused SW GrIS where virtually all meltwater enters moulins or crevasses (Smith et al., 2015; Yang et al., 2016), unlike the present study of NW Greenland.

Unlike the SW GrIS, supraglacial streams and rivers on the NW GrlS are rarely interrupted by moulins or crevasses. Instead, they flow directly over the bare ice surface to its edge, where their flows supply proglacial Minturn River (Fig. 1). On the NW GrIS, the ablation zone therefore tends to form coupled supraglacial-proglacial drainage systems, as exemplified by our study site at Inglefield Land (Fig. 2**a**). Owing to the absence of en- and sub-glacial runoff capture, supraglacial drainage processes controls the routing of meltwater to the ice terminus thus providing the opportunity to validate climate/SMB models directly from proglacial river discharge, without interference from en- and sub-glacial storages and/or delays.

In this study, we investigate the coupled supraglacial-proglacial drainage system of Inglefield Land, NW GrlS by integrating satellite observations and runoff as simulated by two climate/SMB models (Modèle Atmosphérique Régional, MAR v3.11, and Modern-Era Retrospective Analysis for Research and Applications, MERRA-2) over the 2016–2019 melt seasons. First, we use multi-temporal Sentinel-2 and Landsat-8 images to map this coupled drainage system and its seasonal and inter-annual spatio-temporal variations. Then, we correlate these satellite observations with simultaneous and lagged modeled daily runoff, to characterize optimal meltwater routing lag times of supraglacial and proglacial channel networks. Finally, we discuss the implications of the Inglefield Land coupled supraglacial-proglacial drainage system for estimating the GrIS meltwater to the ocean and validating climate/SMB modeled runoff.

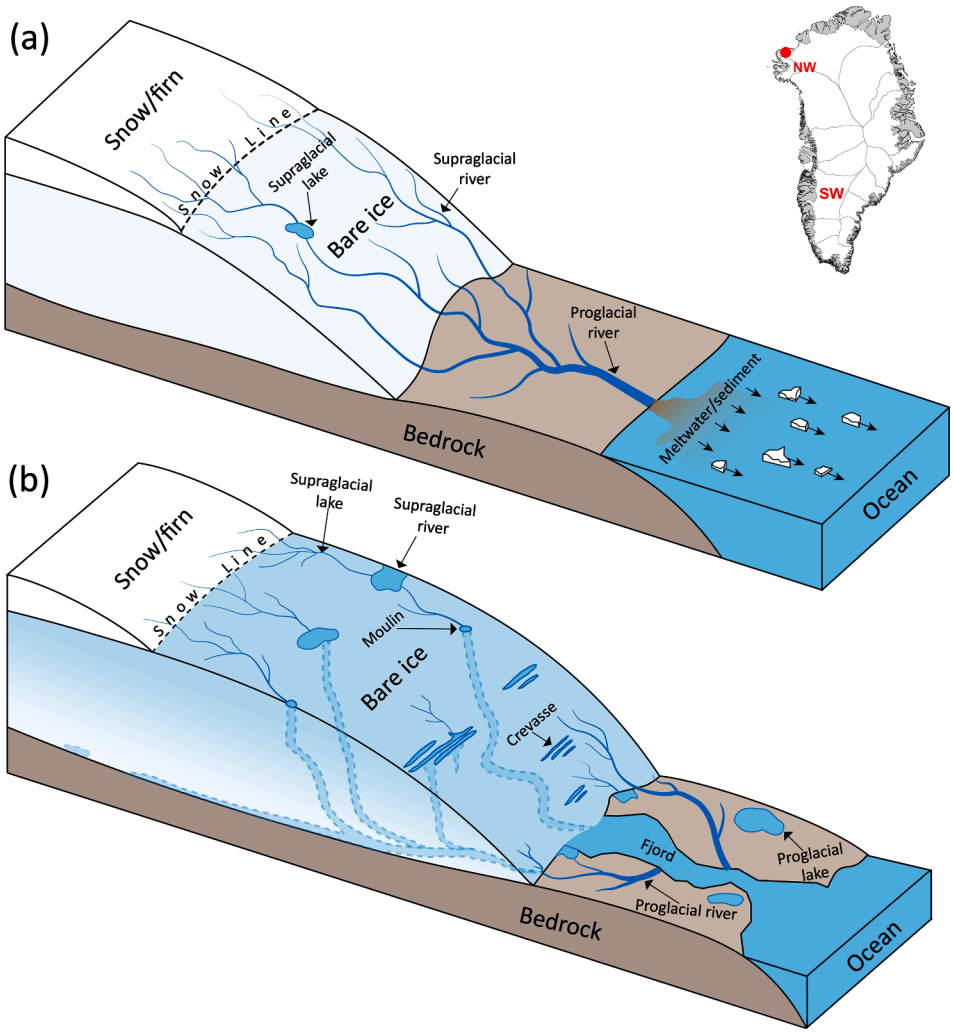

Fig. 1. Schematic of surface meltwater routing process (a) at Inglefield Land (red point in the insert map), NW GrIS where supraglacial streams/rivers are uninterrupted by moulins and crevasses on the ice surface, and (b) on the SW GrIS where virtually all surface meltwater enters moulins or crevasses prior to reaching the proglacial zone.

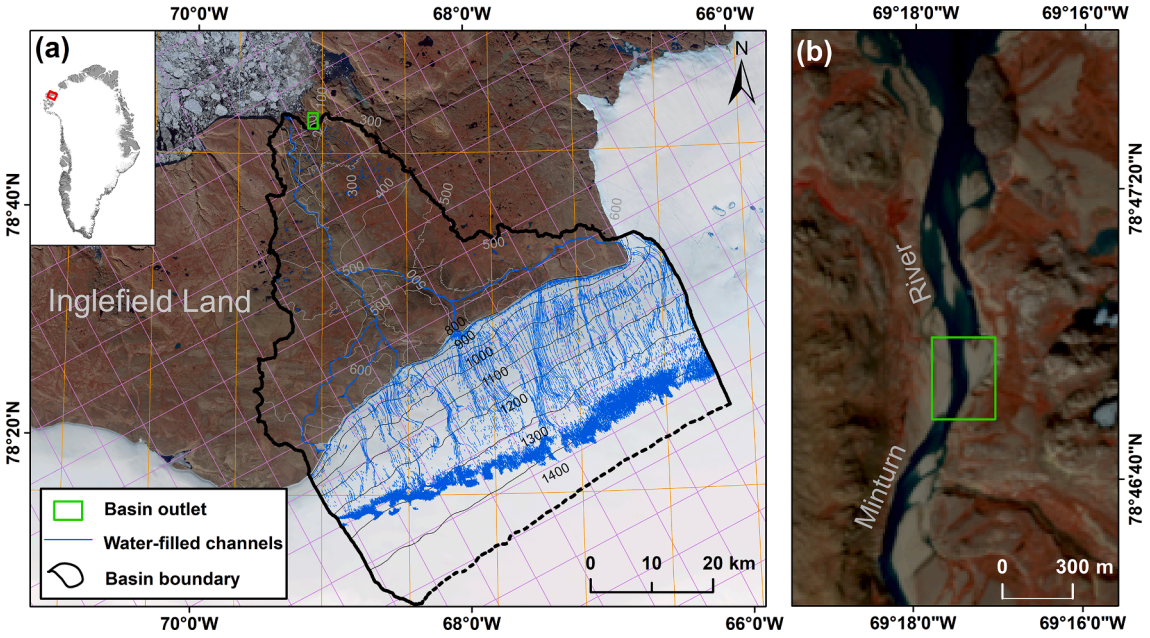

Fig. 2. (a) Coupled supraglacial-proglacial drainage system of Inglefield Land, NW Greenland. Black dashed line represents the upper limit of supraglacial stream migration over the 2016–2019 study period. Purple and orange grids represent the MAR and MERRA-2 grid cells, respectively; (b) Proglacial river effective width (W_e) variations were retrieved within the green rectangle (270 m × 350 m). Stream delineations and image background are from a Sentinel-2 image acquired on July 27, 2019.

2. Study area and data sources

2.1. Study area

A continuous, ~3,400 km^2 supraglacial-proglacial drainage catchment connects the NW GrIS ablation zone to the Nares Strait at Inglefield Land (78°00′ N–78°50′ N, 65°40′ W–69°40′ W, Fig. 2**a**). The supraglacial portion comprises ~2,000 km^2, with elevations gently sloping (~0.02 m/m) from ~1,400 m at the upper limit of supraglacial stream formation to ~600 m at the ice terminus. The equilibrium line altitude (ELA) in this area averaged ~1,100 m from 1991 to 2017 (Noël et al., 2019), and the late-summer snowline averaged ~1,000 m from 2016 to 2017 (Ryan et al., 2019). The proglacial portion comprises ~1,400 km^2, with elevations descending from 600 m to 10 m with a mean slope of ~0.06 m/m. The coastal outlet of the coupled supraglacial-proglacial catchment is ~45 km downstream of the ice edge (Fig. 2**a**). To characterize proglacial river discharge variability at this outlet, we selected a 270 m wide × 350 m long river reach study area (Fig. 2**b**) suitable for repeat satellite imaging as per Smith et al. (1995, 1996). This river reach is located > 1 km away from the ocean and therefore unaffected by ocean tides (Fig. S1) (Wright, 1977).

2.2. Data sources

Ninety-two scenes of 10-m resolution Sentinel-2 Multispectral Instrument (MSI) images and 45 scenes of 30-m resolution Landsat-8 Operational Land Imager (OLI) images, all with cloud cover < 10%, were used to map the Inglefield Land coupled supraglacial-proglacial drainage system during the 2016–2019 melt seasons (Table S1). Two widely-used climate/SMB models, MAR v3.11 forced by the ERA5 reanalysis (Fettweis et al., 2020) and MERRA-2 (3-Hourly, Time-Averaged, Single-Level, Assimilation, Land Ice Surface Diagnostics V5.12.4, M2T3NXGLC, Gelaro et al. (2017)) datasets, were employed to simulate daily surface runoff. The spatial resolution of MAR v3.11 is 7.5 × 7.5 km, while that of MERRA-2 is 0.5° × 0.625° (~56 × 28 km). The MERRA-2 land surface product (1-Hourly, Time-Averaged, Single-Level, Assimilation, Land Surface Diagnostics V5.12.4, M2T1NXLND) was used to compute terrestrial runoff in the proglacial zone. ArcticDEM, a high-resolution 10 m pan-Arctic topography dataset derived from high-resolution stereo images (Porter et al., 2018) and freely available from http://arcticdem.org, was used to extract topographic catchment boundaries on the ice surface and proglacial zone (Table S1).

3. Methods

3.1. Delineation of supraglacial and proglacial channels

Multi-temporal maps of actively flowing supraglacial and proglacial channels were extracted using Sentinel-2 and Landsat-8 images as follows. First, a Normalized Difference Water Index (NDWI = (GREEN – NIR)/(GREEN + NIR)) was used to enhance the contrast between surface water features and image backgrounds (McFeeters, 1996). Two global thresholds of 0.1 and 0.03 were used to extract large proglacial rivers from Sentinel-2 and Landsat-8 NDWI images, respectively. As supraglacial streams are much narrower than proglacial rivers, an additional step of linear feature enhancement (Yang et al., 2015) was applied to extract them. Specifically, a band-pass filter ramped between 1/200 m^{-1} and 1/40 m^{-1} was used to remove low-frequency backgrounds and high-frequency noises in the NDWI images. Next, a Gabor filter with a thickness of 2 pixels was used to enhance the cross-sections of narrow stream channels. To enhance the longitudinal continuity of short stream channels, a path opening operator with a minimum path length of 20 pixels was then applied. Finally, a global threshold (20 out of 255 for both Sentinel-2 and Landsat-8 images) was applied to extract water-occupied supraglacial streams.

3.2. Supraglacial meltwater area fractions and proglacial river effective widths

Two remotely sensed surface water metrics (supraglacial meltwater area fraction and proglacial river effective width) were used to quantify the spatio-temporal variations of supraglacial and proglacial water-filled channels mapped in the Sentinel-2 and Landsat-8 images. Supraglacial meltwater area fraction (A_m) is defined as surface meltwater area

divided by total supraglacial portion area (~2,000 km^2), and has previously been used to quantify supraglacial lake (Sundal et al., 2009) and river (Yang et al., 2021) area variations on the SW GrIS. Proglacial river effective width (W_e), a reach-averaged measure of river width, was calculated following Smith et al. (1995):

$$W_e = A/L \quad (1)$$

where W_e is effective width; and A is the inundation area mapped within a user-defined river reach of length L. Effective width has proven to be a reliable indicator of river discharge variations in braided and single channel rivers (Smith et al., 1995, 1996; Smith, 1997; Bjerklie et al., 2005; Ashmore and Sauks. 2006; Gleason et al., 2015; Gaurav et al., 2021) and thereby we used it to characterize proglacial river discharge. The length L of the selected proglacial river reach is 350 m, ~6x the typical river width (~60 m, Fig. 2**b**). This length is sufficiently long to provide a stable width-discharge relationship (Bjerklie et al., 2005; Smith and Pavelsky, 2008).

To create multi-sensor time series of A_m and W_e, we compared subsets of contemporaneous Sentinel-2 and Landsat-8 images (n = 8 image pairs on the ice sheet; n = 20 image pairs in the proglacial zone) and found strong positive linear correlations between them (r^2 = 0.90 and 0.87 for W_e and A_m, respectively, $p < 0.01$, Fig. 3). Using these regression equations, Sentinel-2 metrics were used as references to adjust the corresponding Landsat-8 metrics, creating integrated time series of A_m and W_e using both satellite platforms.

3.3. Calculating modeled surface meltwater runoff

Outputs of daily ice surface runoff (mm/day) from MAR v3.11 and MERRA-2 were obtained for the 2016–2019 melt seasons (July 1–August 30 of each year). Total ice surface runoff within the coupled supraglacial basin was calculated by intersecting MAR v3.11 and MERRA-2 grid cells (7.5 × 7.5 km and ~56 × 28 km, respectively) with the ice surface basin boundary and summing the intersected runoff value (Smith et al., 2017; Pitcher et al., 2020). In MAR v3.11, the runoff value of each grid cell was calculated from other MAR v3.11 components as per Lenaerts et al. (2019). The integrated modeled ice surface runoff was then compared with supraglacial meltwater area fraction A_m.

To compare modeled runoff with proglacial river effective width W_e, daily proglacial terrestrial runoff within the 1,400 km^2 proglacial zone was computed from MAR v3.11 and MERRA-2 and added to ice surface runoff. We then used the total modeled runoff to compare with satellite-derived W_e. Owing to the general aridity of the Inglefield Land proglacial zone, proglacial terrestrial runoff only account for ~0.5–13% of the total runoff in MAR v3.11 and MERRA-2 (Table 1) and have limited contributions to W_e.

3.4. Calculating meltwater routing lag time

At least several days, if not more, are typically required to route GrIS surface meltwater from the ice surface to the ocean (Mernild and Hasholt, 2009; Rennermalm et al., 2013; Smith et al., 2017; van As et al., 2017). To quantify NW GrIS surface meltwater routing lag times at Inglefield Land, we created varying lagged modeled runoff using a plausible range of time lags (2–10 days) as per Zuo and Oerlemans (1996):

$$\frac{dW}{dt} = -\frac{W}{t^*} \quad (2)$$

where $\frac{dW}{dt}$ is the lagged runoff and t^* is the variable lag time (one day as time step). The computed lagged runoff was then separately compared with satellite-derived A_m and W_e. The highest correlation between lagged runoff and both satellite metrics was identified as the most likely meltwater routing lag time. Specifically, the highest produced r^2

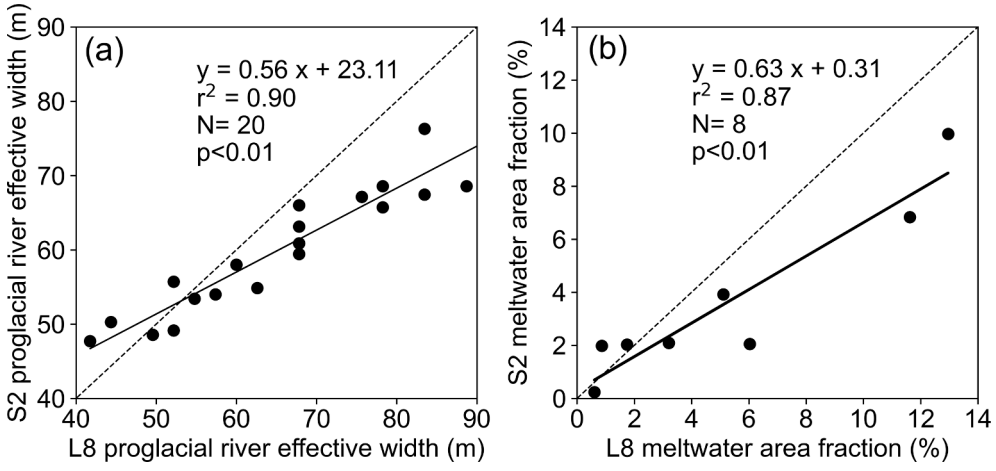

Fig. 3. Correlations of (a) proglacial river effective width (W_e); and (b) supraglacial meltwater area fraction (A_m) as derived from same-day Sentinel-2 and Landsat-8 images. A total of 8 pairs of same-day S2/L8 images on the ice sheet and 20 image pairs of same-day S2/L8 images in the proglacial zone were acquired over our study area from 2016 to 2019. Strong correlations between S2 and L8 retrievals enable correction integrated times series of W_e and A_m using both satellite sensors.

Table 1
Surface runoff estimated from MAR and MERRA-2 models from July to August on the NW GrIS.

Model	Year	Average ice surface runoff (mm/day)	Total proglacial runoff (10^6 m^3/s)	Total runoff (10^6 m^3/s)	Total proglacial runoff/Total runoff (%)
MAR	2016	11.16	0.08	1.49	5.4
	2017	4.86	0.07	0.69	10.1
	2018	3.54	0.05	0.49	10.2
	2019	15.02	0.01	1.90	0.5
MERRA-2	2016	5.49	0.06	0.76	7.9
	2017	2.26	0.01	0.30	3.3
	2018	2.60	0.02	0.35	5.7
	2019	7.53	0.14	1.08	12.9

between lagged runoff and A_m corresponds to the optimal supraglacial lag time; the highest produced r^2 between lagged runoff and W_e corresponds to the optimal "bulk" lag time (i.e. the combined delay of both supraglacial and proglacial flow routings).

4. Results

4.1. Satellite mapping of supraglacial and proglacial surface water

Water-filled supraglacial and proglacial stream/river channels were mapped 40 and 63 times, respectively, during the 2016–2019 melt seasons, yielding corresponding average revisit intervals of ~6 d and ~4 d from July 1 to August 31. The mapped supraglacial streams are approximately subparallel with high drainage density (typically spaced ~100 m apart, Figs. 4 and S3), consistent with a previous study of this area (Yang et al., 2019b). Our multi-temporal mapping results also confirm that the supraglacial streams route surface meltwater directly off the ice sheet to the proglacial rivers, with no capture by moulins and crevasses (Figs. 4–5 and S3–S4).

Each summer, actively flowing supraglacial streams progressively expand from low to high elevations (~1,400 m) before retreating to low elevations (Figs. 4 and S3). This observation of significant seasonal spatio-temporal variations is consistent with previous findings reported for the SW GrIS (Lampkin and Vanderberg, 2014; Yang et al., 2021). Similarly, the areal extent of the actively flowing proglacial rivers first increases then decreases (Figs. 5–6 and S4), consistent with the seasonal surface meltwater runoff cycle (Fettweis et al., 2020; Mankoff et al., 2020). At this broadly seasonal time scale, MAR and MERRA-2 runoff simulations track these satellite-derived surface water metrics for all four melt seasons rather well (Fig. 6).

Average daily MAR ice surface runoff is significantly higher during the two warmer summers (11.2 mm/day in 2016 and 15.0 mm/day in 2019) than during the two cold summers (4.9 mm/day in 2017 and 3.5 mm/day in 2018) (Fig. 6 and Table 1). MERRA-2 performs similarly and predicts higher average daily ice surface runoff in 2016 (5.5 mm/day) and 2019 (7.5 mm/day) and lower values in 2017 (2.3 mm/day) and 2018 (2.6 mm/day). Average temperature is also significantly higher during the two warmer summers (-0.6 °C in 2016 and 0.52 °C in 2019) than during the two cold summers (-2.2 °C in 2017 and -2.3 °C in 2018). These overall runoff simulations are corroborated by satellite-derived A_m and W_e, which are larger during the two warm summers. For example, average A_m is ~10% and W_e is ~75 m in the warm summers, but just ~4% and ~70 m, respectively, in the cold summers (Fig. 6). Similarly, water-filled supraglacial streams migrate to higher elevations (~1,400 m) in the two warm summers than in the two cold summers (~1,300 m, Figs. 4 and S3).

4.2. Meltwater routing through the coupled supraglacial-proglacial drainage system

Supraglacial streams and proglacial rivers were mapped contemporaneously 36 times during the 2016–2019 melt seasons. During these days, we find that A_m and W_e are strongly correlated ($r^2 = 0.85$, $p < 0.01$, Fig. 7**a**). This confirms that the coupled supraglacial-proglacial drainage system routes meltwater efficiently from the ice surface to the proglacial zone (Yang et al., 2019b). A weaker correlation between the supra- and pro-glacial portions of the system would be expected if surface meltwater was being impounded in lakes, or stored en- and sub-glacially (Rennermalm et al., 2013; Cooper et al., 2018).

These two satellite-derived surface water metrics are also positively correlated with modeled runoff (Figs. 7**b**–7**c**), in line with previously reported high correlation ($r^2 = 0.89$) between A_m and modeled runoff on the SW GrIS (Yang et al., 2021). This result confirms that MAR and MERRA-2 reliably simulate variations of surface meltwater runoff at the broadly seasonal time scale, both on the ice surface and proglacial zone. However, correlations of modeled runoff with satellite-derived A_m ($r^2 = 0.81$ and 0.66 for MAR and MERRA-2, respectively, Fig. 7**b**) and W_e ($r^2 = 0.77$ and 0.64 for MAR and MERRA-2, respectively, Fig. 7**c**) are slightly lower than the correlation for two satellite-derived surface water metrics ($r^2 = 0.85$, Fig. 7**a**). We suggest that these slightly lower correlations signify that modeled runoff does not perfectly match satellite observations of surface water extent, supporting previous reports of timing mismatches between modeled and observed GrIS runoff (Smith et al., 2017; Yang et al., 2019a).

Moreover, correlations of A_m with modeled runoff ($r^2 = 0.81$ and 0.66 for MAR and MERRA-2, respectively, Fig. 7**b**) are somewhat higher

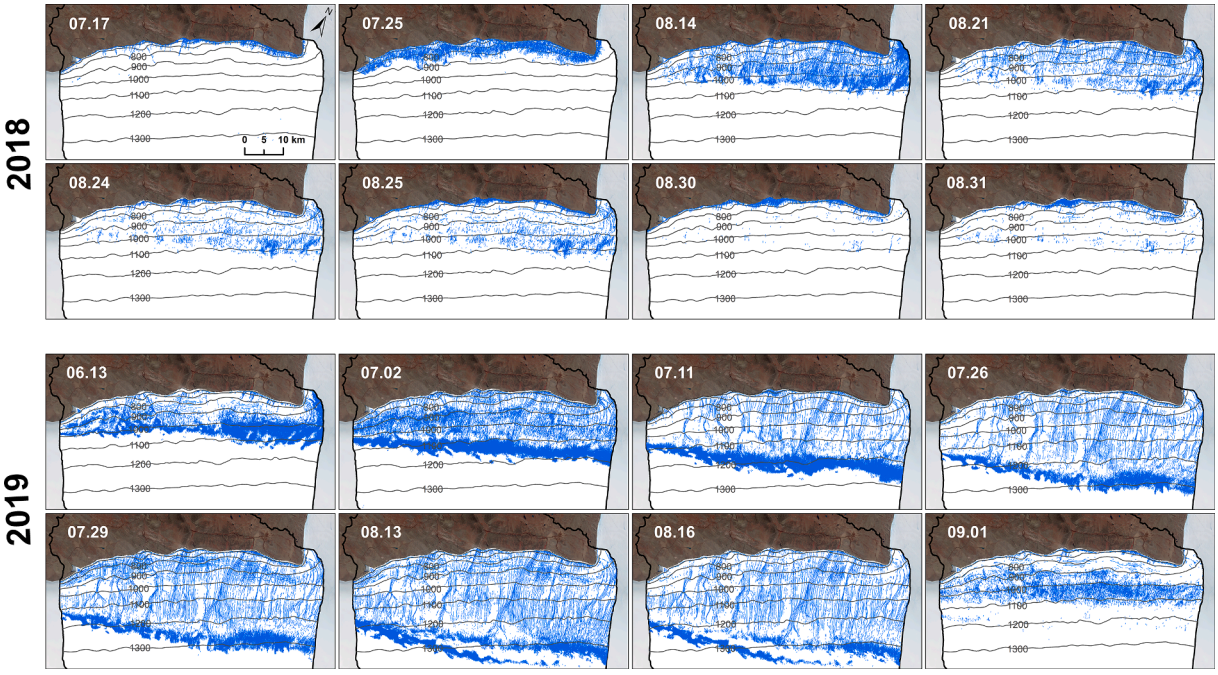

Fig. 4. Seasonal evolution of supraglacial stream drainage pattern during the 2018 and 2019 melt seasons mapped from Sentinel-2 images. Each summer, supraglacial streams progressively expand from low to high elevations before retreating to low elevations. For 2016 and 2017 melt seasons see Figure S3.

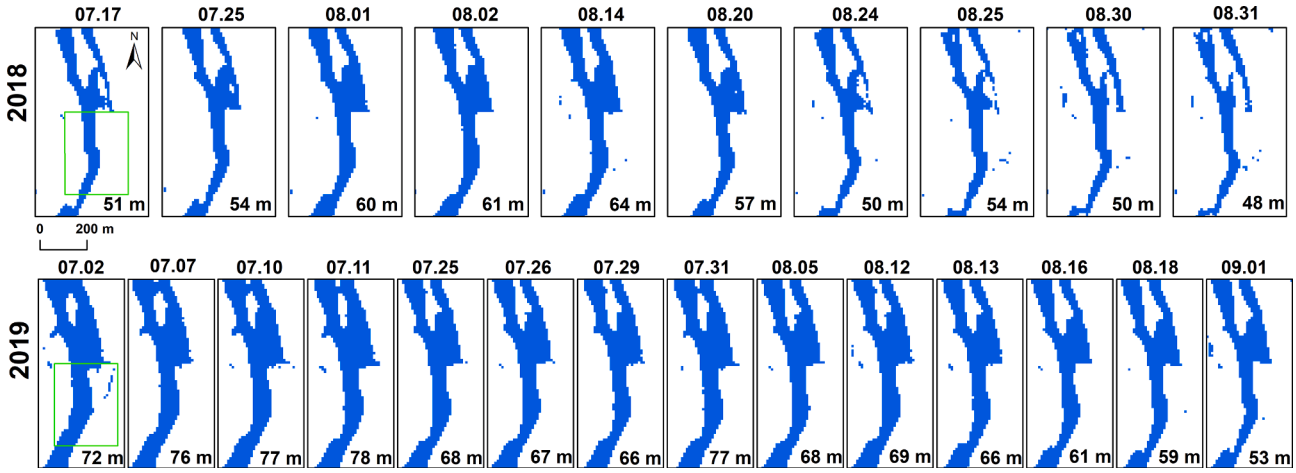

Fig. 5. Seasonal evolution of proglacial river width at the basin outlet during the 2018 and 2019 melt seasons, here mapped using Sentinel-2 images. The inundated river planform first increases then decreases. River effective width (W_e) is calculated as the ratio of water surface area to the reach length (350 m, green rectangle) following Smith et al. (1995, 1996). For 2016 and 2017 effective widths see Figure S4.

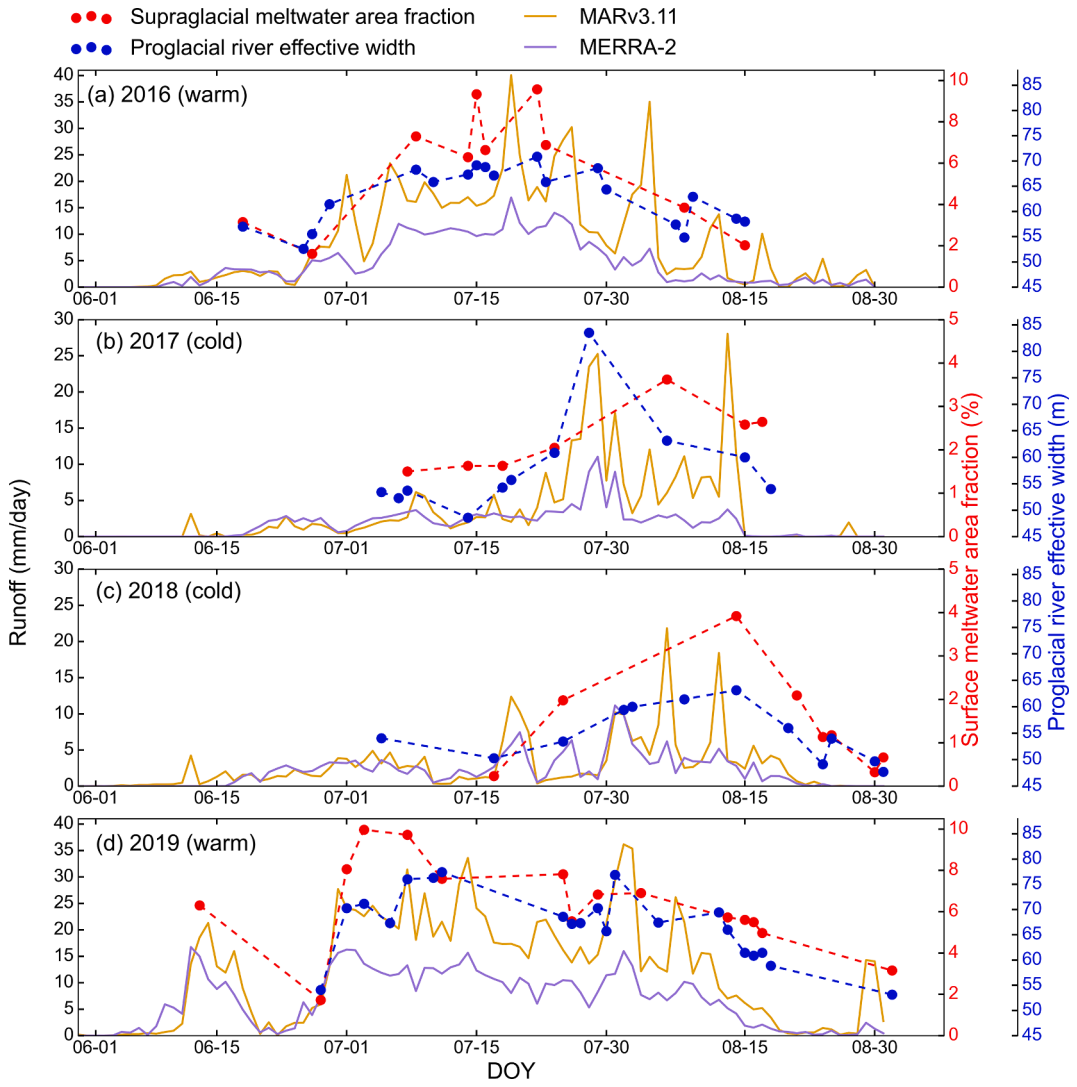

Fig. 6. Seasonal evolution of satellite-derived supraglacial meltwater area fraction (A_m) and proglacial river effective width (W_e) during the 2016–2019 melt seasons (a) – (d). MAR and MERRA-2 runoff broadly track satellite-derived A_m and W_e for all four melt seasons.

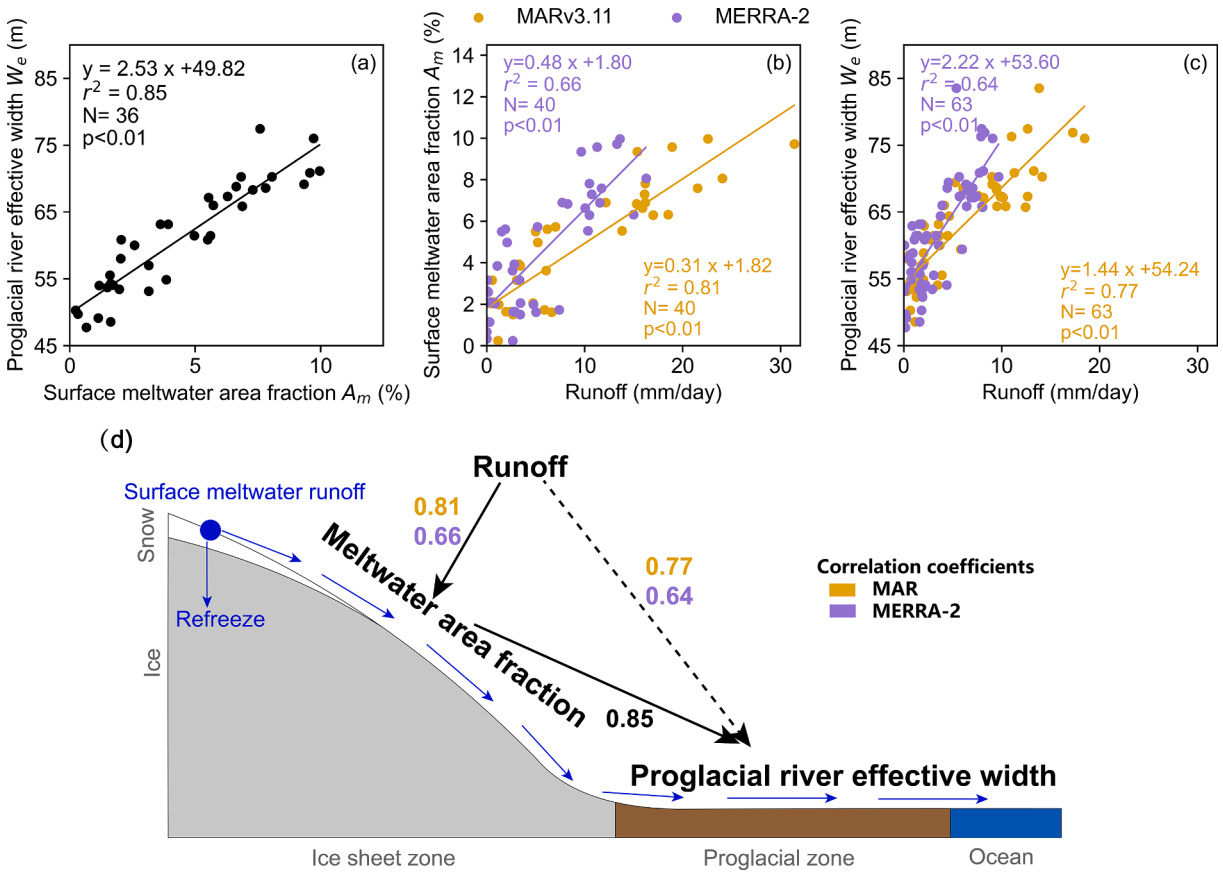

Fig. 7. Correlations between satellite-derived supraglacial meltwater area fraction (A_m) and proglacial river effective width (W_e) and modeled runoff across all four melt seasons (2016–2019). Runoff in panel (c) is the sum of ice surface and proglacial terrestrial runoff.

those for W_e (r^2 = 0.77 and 0.64 for MAR and MERRA-2, respectively, Fig. 7**c**). This signifies that climate/SMB models may simulate the timing of runoff on the ice surface (higher r^2 of A_m-runoff) slightly better than proglacial runoff downstream (lower r^2 of W_e-runoff), an expected result owing to the absence of lateral flow routing in the climate/SMB models (Rennermalm et al., 2013; van As et al., 2017). Remotely sensed surface meltwater mapping (Figs. 4 and 5) and quantitative metrics (Figs. 6 and 7), therefore, can broadly validate climate/SMB modeled runoff timing at seasonal time scale.

4.3. *Surface meltwater runoff routing lag time*

By correlating lagged (2–10 d) runoff with satellite observations, we further estimate optimal (i.e. yielding the highest r^2) lag times of ~2 days for both A_m (r^2 = 0.87) and W_e (r^2 = 0.82) from MAR (Figs. 8 and 10), and the optimal lag times of ~5 days for A_m (r^2 = 0.87) and ~4 days for W_e (r^2 = 0.69) from MERRA-2 (Figs. 9 and 10). Because the "bulk" (i.e. the combined delays of both supraglacial and proglacial flow routing) lag time estimated from W_e should be longer than supraglacial lag time estimated from A_m, we thereby suggest that the routing lag times estimated from MERRA-2 are problematic and focus instead on lag times estimated from MAR.

The optimal "bulk" lag time is thus 2 days, while the optimal supraglacial lag time is also 2 days from MAR. We conclude that supraglacial flow routing accounts for most of the bulk lag time whereas proglacial flow routing is much shorter (<1 day). This finding is consistent with previous studies indicating short lag time (i.e. several hours) in proglacial rivers on the SW GrIS (van As et al., 2017; Smith et al., 2021). However, we cannot quantify the lag time at hourly time scales due to the limited temporal resolution of climate/SMB models and satellite image acquisitions in this study. Nevertheless, the combination of remote sensing and climate/SMB models, therefore, enables approximation of meltwater routing lag times through coupled supraglacial-proglacial drainage systems.

5. Discussion

5.1. *NW GrIS supraglacial streams are continuous and form at high elevations*

The observed strongly positive correlation (r^2 = 0.85, Fig. 7) between satellite-derived supraglacial meltwater area fraction A_m and proglacial river effective width W_e signifies that the coupled supraglacial-proglacial drainage system directly and efficiently routes surface meltwater from the ice surface to the ocean (Fig. 1). The Inglefield Land supraglacial channel network is characterized by elongated (up to 20 km), roughly parallel supraglacial streams that convey meltwater to the ice edge uninterrupted by moulins or crevasses capture (Figs. 4 and S3).

Therefore, this area of the NW GrIS ablation zone differs significantly from the SW GrIS (Fig. 1), where virtually all supraglacial streams flow into moulins or crevasses before reaching the proglacial zone (Smith et al., 2015; Yang et al., 2016). We conclude that the supraglacial-proglacial drainage system at Inglefield Land supplies little to no water to the bed; and that Inglefield Land proglacial river discharges reflect mostly ice sheet meltwater runoff with little to no mixing with subglacial water from the bed. Furthermore, owing high aridity, the proglacial zone contributes only modest (here 0.5 – 13%) terrestrial runoff to remotely sensed W_e. As a practical matter, this signifies that proglacial river discharge in this area offers an attractive target for validating climate/SMB model surface runoff simulations, obviating the need to conduct brief, logistically challenging streamflow gauging

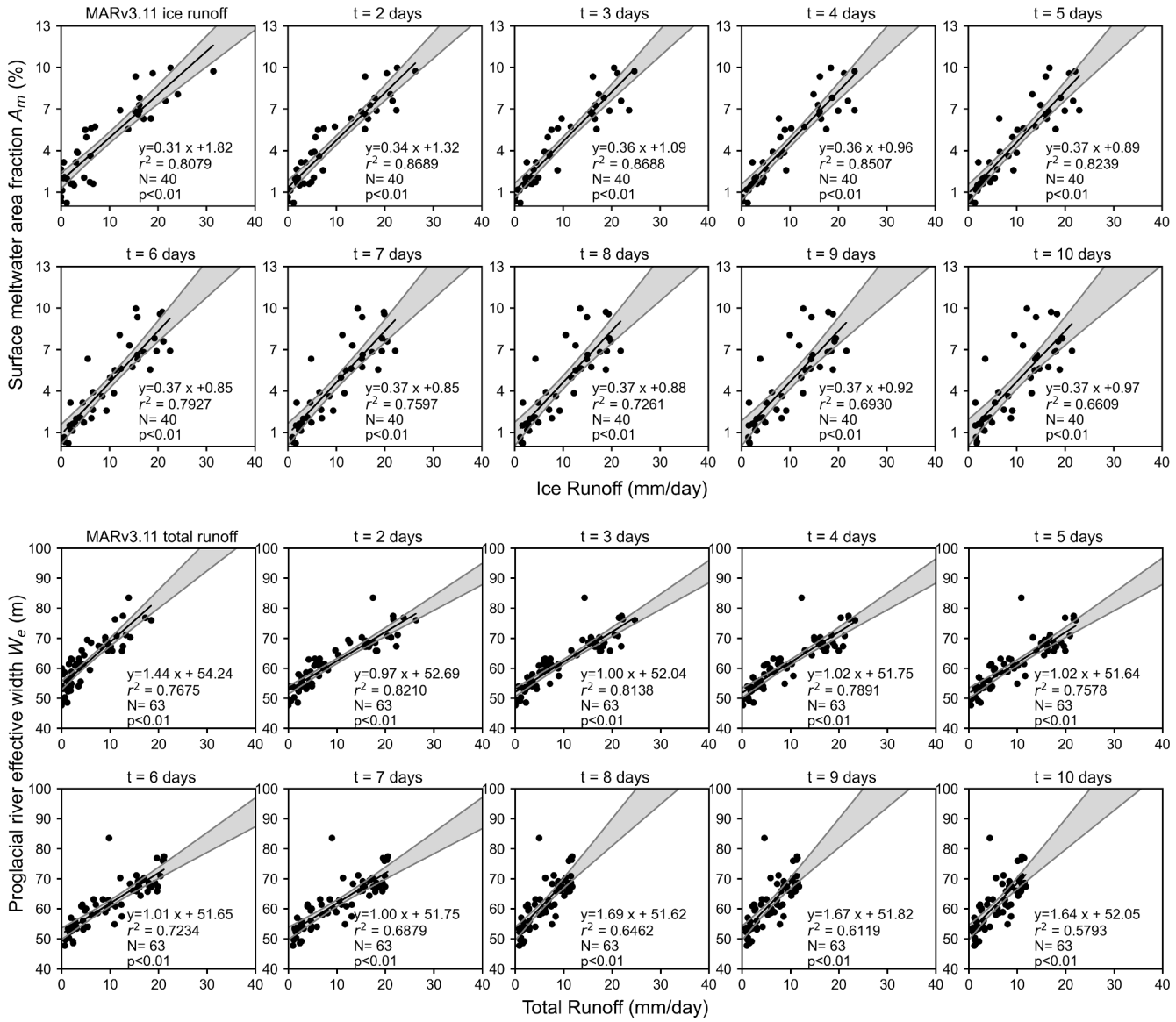

Fig. 8. Comparison between lagged (2–10 days) MAR runoff with satellite-derived supraglacial meltwater area fraction (A_m, upper two rows) and proglacial river effective width (W_e, bottom two rows). Highest correlation between MAR runoff and both satellite-derived surface water metrics ($r^2 = 0.87$ and 0.82 for A_m and W_e, respectively) is acquired at ~2 days.

expeditions on the ice surface (e.g. Smith et al. (2015, 2017)). Furthermore, the ice sheet portion area (~2,000 km^2) of the Inglefield Land coupled supraglacial-proglacial drainage catchment is far larger than most supraglacial catchments of the SW GrIS (i.e. 0.4–244.9 km^2, Yang and Smith (2016)), allowing readier comparison with coarse-resolution (~10^0–10^1 km) climate/SMB model output.

The upper elevation limit of supraglacial stream extent (~1,300 m in 2016 and ~1,200 m in 2017) is notably higher than the maximum snowline elevation observed on the ice surface (~1,053 m and ~1,006 m in 2016 and 2017, respectively, Ryan et al. (2019)). This finding of channelized meltwater above the bare-ice ablation zone suggests that the NW GrIS snow/firn may have low permeability (MacFerrin et al., 2019), thereby enabling supraglacial stream formation at higher elevations.

5.2. *Implication of NW GrIS surface meltwater runoff simulations and observations*

On the ice sheet surface, positive linear relationships are found between modeled runoff and satellite-derived supraglacial meltwater area fraction A_m (Fig. 7**b**). This signifies that climate/SMB models track ice surface meltwater well at the seasonal time scale. Moreover, A_m is readily calculated from satellite images with high accuracy and is thus an effective metric for evaluating runoff simulations from climate/SMB models.

The correlation of W_e and modeled runoff decreases to 0.77 for MAR and 0.64 for MERRA-2 (Fig. 7**c**), implying that the timing of surface meltwater runoff changes after entering the proglacial river. Although W_e does not quantify proglacial river discharge in absolute terms, the correlations of W_e-runoff presented here are comparable to previously reported values for the SW GrIS. For example, a correlation of $r^2 = 0.62$, was obtained between output from the Surface Energy Balance (SEB) model and in situ proglacial river discharge measurements (van As et al., 2012), and a correlation of $r^2 = 0.72$ was found between SnowModel ERA-I modeled runoff and in situ proglacial river discharge measurements (Mernild et al., 2018). These comparable correlations acquired from both in situ proglacial discharge measurements on the SW GrIS and the satellite-derived W_e on the NW GrIS suggest remote sensing

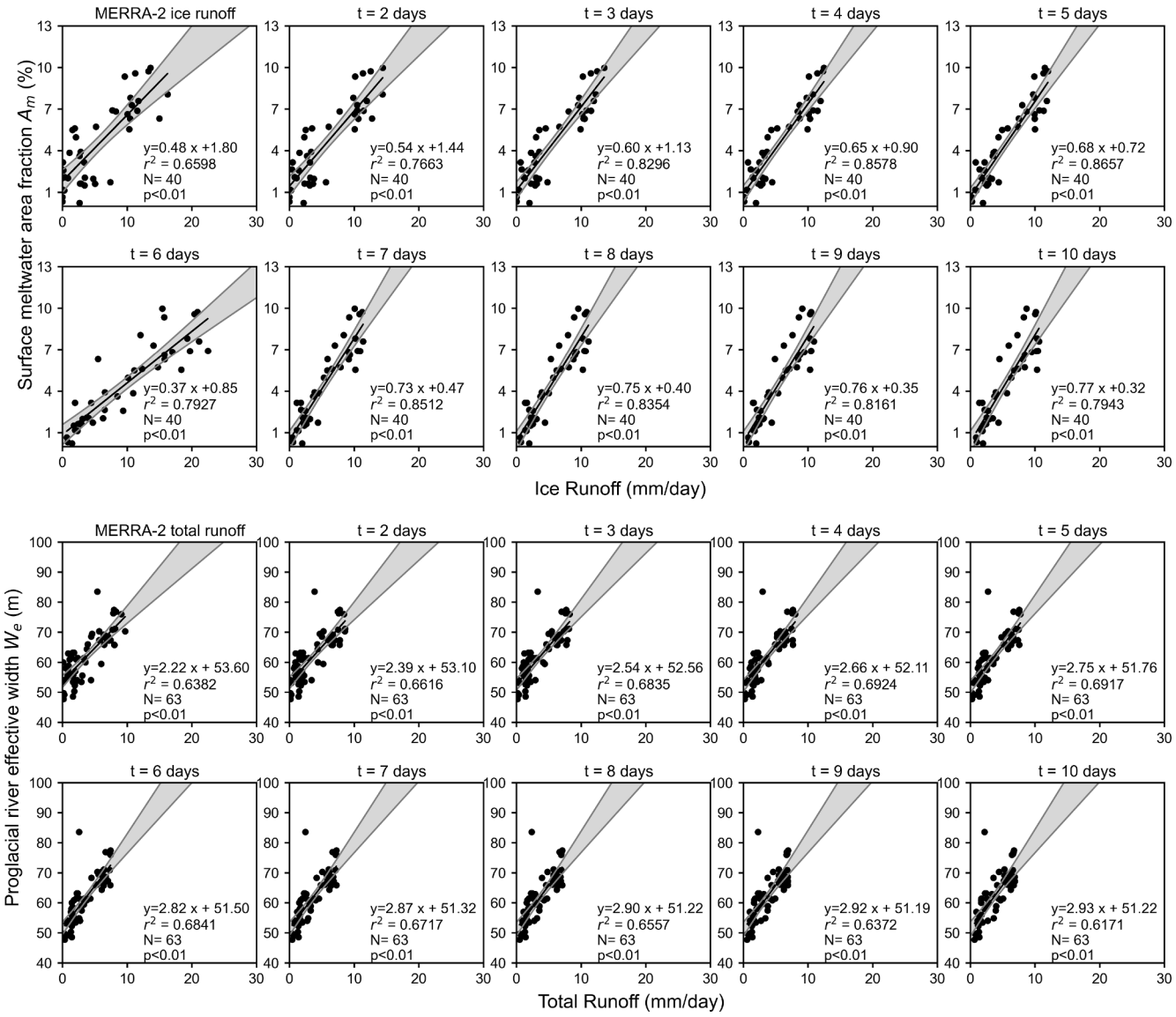

Fig. 9. Comparison between lagged (2–10 days) MERRA-2 runoff with satellite-derived supraglacial meltwater area fraction (A_m, upper two rows) and proglacial river effective width (W_e, bottom two rows). Highest correlation for MERRA-2 runoff and satellite-derived A_m ($r^2 = 0.87$) is acquired at ~5 days; highest correlation for MERRA-2 runoff and satellite-derived W_e ($r^2 = 0.69$) is acquired at ~4 days.

retrievals are useful for validating the seasonal timing of runoff simulations from climate/SMB models.

5.3. Interrogation of climate/SMB model surface runoff simulations

MAR and MERRA-2 runoff simulations exhibit somewhat different correlations with satellite-derived surface water metrics, with MAR ($r^2 = 0.81$ for A_m and 0.77 for W_e) more strongly correlated than MERRA-2 (0.66 for A_m and 0.64 for W_e, **see** Figs. 7**b**–7**c**). As a result, MERRA-2 runoff yields lower correlations with both satellite-derived surface water metrics and also fails to estimate supraglacial and proglacial routing lag times. We suggest this is mainly attributed to the spatial resolution of MERRA-2 (~56 × 28 km), which is much lower than that of MAR (7.5 × 7.5 km, Fig. 2**a**). The marginal grid cells of MERRA-2 thus occupy greater area (~45% of all grid cells used) than those of MAR (~20% of all grid cells used) and these marginal grid cells are known to simulate runoff with large uncertainties (Vernon et al., 2013; Mankoff et al., 2020).

We therefore suggest caution when interpreting low-resolution (>10 km) climate/SMB model output to coupled supraglacial-proglacial drainage systems, even the relatively large one (~3,400 km^2) examined here for Inglefield Land. Future studies should consider applications of downscaling techniques (Franco et al., 2012; Noël et al., 2016) when applying climate/SMB model output near the ice sheet edge.

6. Conclusions

This study investigates the coupled supraglacial-proglacial drainage system of Inglefield Land, NW GrlS by integrating Sentinel-2 and Landsat-8 satellite images with surface runoff simulations from two climate/SMB models (MAR and MERRA-2). We find: 1) the coupled supraglacial-proglacial drainage system routes meltwater directly and efficiently from the ice surface to the ocean without contacting the bed; 2) densely-spaced, subparallel supraglacial streams develop above the snowline and flow continuously to the ice edge, unlike SW GrlS; and 3) the coupled supraglacial-proglacial drainage system exhibits seasonal and inter-annual areal variations that may be used to evaluate climate/SMB model runoff simulations. Comparison of satellite observations with MAR and MERRA-2 runoff reveals that ~2 d is required to evacuate meltwater from the ice surface to the ocean; and that most of this transit

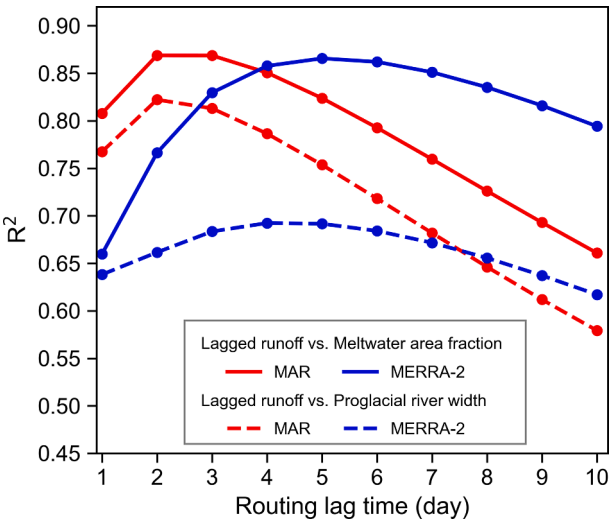

Fig. 10. Variations in r^2 between lagged (2–10 days) MAR and MERRA-2 runoff simulations and satellite-derived supraglacial meltwater area fraction (A_m) and proglacial river effective width (W_e).

time occurs on the ice surface rather than in the proglacial zone. Satellite remote sensing of the ice-land drainage system at Inglefield Land thus enables observations and tracking of NW GrIS meltwater runoff, from source to the Nares Strait and global ocean.

CRediT authorship contribution statement

Ya Li: Conceptualization, Methodology, Formal analysis, Investigation, Writing – original draft, Visualization. **Kang Yang:** Conceptualization, Methodology, Investigation, Writing – review & editing, Supervision, Funding acquisition. **Shuai Gao:** Formal analysis, Investigation, Writing – review & editing. **Laurence C. Smith:** Conceptualization, Investigation, Writing – review & editing. **Xavier Fettweis:** Conceptualization, Investigation, Writing – review & editing. **Manchun Li:** Supervision, Funding acquisition.

Declaration of Competing Interest

The authors declare that they have no known competing financial interests or personal relationships that could have appeared to influence the work reported in this paper.

Data availability

Daily MAR (Modèle Atmosphérique Régionale) 3.11 model data can be accessed by contacting Xavier Fettweis (xavier.fettweis@uliege.be). MERRA-2 model data can be accessed via https://disc.gsfc.nasa.gov/datasets. The supraglacial stream detection codes are freely available at https://github.com/njuRS/River_detection.

Acknowledgements

Ya Li and Kang Yang acknowledge support from the National Natural Science Foundation of China (41871327), the Strategic Priority Research Program of the Chinese Academy of Sciences (XDA19070201), the Frontiers Science Center for Critical Earth Material Cycling Fund (JBGS2102), and the Fundamental Research Funds for the Central Universities (14380097). Laurence C. Smith acknowledges support from the NASA Cryospheric Science Program (80NSSC19K0942) managed by Dr. Thorsten Markus. ArcticDEMs were provided by the Polar Geospatial Center at the University of Minnesota under NSF-OPP awards 1043681, 1559691, and 1542736.

Appendix A. Supplementary data

Supplementary data to this article can be found online at https://doi.org/10.1016/j.jag.2021.102647.

References

Ashmore, P., Sauks, E., 2006. Prediction of discharge from water surface width in a braided river with implications for at-a-station hydraulic geometry. Water Resour. Res. 42, W03406.
Bjerklie, D.M., Moller, D., Smith, L.C., Dingman, S.L., 2005. Estimating discharge in rivers using remotely sensed hydraulic information. J. Hydrol. 309 (1-4), 191–209.
Cooper, M.G., Smith, L.C., Rennermalm, A.K., Miège, C., Pitcher, L.H., Ryan, J.C., Yang, K., Cooley, S.W., 2018. Meltwater storage in low-density near-surface bare ice in the Greenland ice sheet ablation zone. Cryosphere 12 (3), 955–970.
Enderlin, E.M., Howat, I.M., Jeong, S., Noh, M.-J., van Angelen, J.H., van den Broeke, M. R., 2014. An improved mass budget for the Greenland ice sheet. Geophys. Res. Lett. 41 (3), 866–872.
Ettema, J., van den Broeke, M.R., van Meijgaard, E., van de Berg, W.J., Bamber, J.L., Box, J.E., Bales, R.C., 2009. Higher surface mass balance of the Greenland ice sheet revealed by high-resolution climate modeling. Geophys. Res. Lett. 36, L12501.
Fettweis, X., Hofer, S., Krebs-Kanzow, U., Amory, C., Aoki, T., Berends, C.J., Born, A., Box, J.E., Delhasse, A., Fujita, K., Gierz, P., Goelzer, H., Hanna, E., Hashimoto, A., Huybrechts, P., Kapsch, M.-L., King, M.D., Kittel, C., Lang, C., Langen, P.L., Lenaerts, J.T.M., Liston, G.E., Lohmann, G., Mernild, S.H., Mikolajewicz, U., Modali, K., Mottram, R.H., Niwano, M., Noël, B., Ryan, J.C., Smith, A., Streffing, J., Tedesco, M., van de Berg, W.J., van den Broeke, M., van de Wal, R.S.W., van Kampenhout, L., Wilton, D., Wouters, B., Ziemen, F., Zolles, T., 2020. GrSMBMIP: intercomparison of the modelled 1980–2012 surface mass balance over the Greenland Ice Sheet. Cryosphere 14 (11), 3935–3958.
Franco, B., Fettweis, X., Lang, C., Erpicum, M., 2012. Impact of spatial resolution on the modelling of the Greenland ice sheet surface mass balance between 1990–2010, using the regional climate model MAR. Cryosphere 6 (3), 695–711.
Gaurav, K., Métivier, F., Sinha, R., Kumar, A., Tandon, S.K., 2021. Coupling threshold theory and satellite-derived channel width to estimate the formative discharge of Himalayan foreland rivers. Earth Surf. Dyn. 9 (1), 47–70.
Gelaro, R., McCarty, W., Suárez, M.J., Todling, R., Molod, A., Takacs, L., Randles, C.A., Darmenov, A., Bosilovich, M.G., Reichle, R., Wargan, K., Coy, L., Cullather, R., Draper, C., Akella, S., Buchard, V., Conaty, A., da Silva, A.M., Gu, W., Kim, G.-K., Koster, R., Lucchesi, R., Merkova, D., Nielsen, J.E., Partyka, G., Pawson, S., Putman, W., Rienecker, M., Schubert, S.D., Sienkiewicz, M., Zhao, B., 2017. The Modern-Era Retrospective Analysis for Research and Applications, Version 2 (MERRA-2). J. Clim. 30 (14), 5419–5454.
Gleason, C.J., Smith, L.C., Finnegan, D.C., LeWinter, A.L., Pitcher, L.H., Chu, V.W., 2015. Technical Note: Semi-automated effective width extraction from time-lapse RGB imagery of a remote, braided Greenlandic river. Hydrol. Earth Syst. Sci. 19 (6), 2963–2969.
Lampkin, D.J., VanderBerg, J., 2014. Supraglacial melt channel networks in the Jakobshavn Isbræ region during the 2007 melt season. Hydrol. Processes 28 (25), 6038–6053.
Lenaerts, J.T.M., Medley, B., Broeke, M.R., Wouters, B., 2019. Observing and modeling ice sheet surface mass balance. Rev. Geophys. 57 (2), 376–420.
MacFerrin, M., Machguth, H., As, D.V., Charalampidis, C., Stevens, C.M., Heilig, A., Vandecrux, B., Langen, P.L., Mottram, R., Fettweis, X., Broeke, M.R.V.D., Pfeffer, W. T., Moussavi, M.S., Abdalati, W., 2019. Rapid expansion of Greenland's low-permeability ice slabs. Nature 573 (7774), 403–407.
Mankoff, K.D., Noël, B., Fettweis, X., Ahlstrøm, A.P., Colgan, W., Kondo, K., Langley, K., Sugiyama, S., van As, D., Fausto, R.S., 2020. Greenland liquid water discharge from 1958 through 2019. Earth Syst. Sci. Data 12 (4), 2811–2841.
McFeeters, S.K., 1996. The use of the Normalized Difference Water Index (NDWI) in the delineation of open water features. Int. J. Remote Sens. 17 (7), 1425–1432.
Mernild, S.H., Hasholt, B., 2009. Observed runoff, jökulhlaups and suspended sediment load from the Greenland ice sheet at Kangerlussuaq, West Greenland, 2007 and 2008. J. Glaciol. 55 (193), 855–858.
Mernild, S.H., Liston, G.E., Van As, D., Hasholt, B., Yde, J.C., 2018. High-resolution ice sheet surface mass-balance and spatiotemporal runoff simulations: Kangerlussuaq, west Greenland. Arct. Antarct. Alp. Res. 50, S100008.
Mouginot, J., Rignot, E., Bjørk, A.A., van den Broeke, M., Millan, R., Morlighem, M., Noël, B., Scheuchl, B., Wood, M., 2019. Forty-six years of Greenland Ice Sheet mass balance from 1972 to 2018. PNAS 116 (19), 9239–9244.
Noël, B., van de Berg, W.J., Machguth, H., Lhermitte, S., Howat, I., Fettweis, X., van den Broeke, M.R., 2016. A daily, 1 km resolution data set of downscaled Greenland ice sheet surface mass balance (1958–2015). Cryosphere 10 (5), 2361–2377.
Noël, B., van de Berg, W.J., Lhermitte, S., van den Broeke, M.R., 2019. Rapid ablation zone expansion amplifies north Greenland mass loss. Sci. Adv. 5 (9) https://doi.org/10.1126/sciadv.aaw0123.
Overeem, I., Hudson, B., Welty, E., Mikkelsen, A., Bamber, J., Petersen, D., Lewinter, A., Hasholt, B., 2015. River inundation suggests ice-sheet runoff retention. J. Glaciol. 61 (228), 776–788.
Pitcher, L.H., Smith, L.C., Gleason, C.J., Miège, C., Ryan, J.C., Hagedorn, B., van As, D., Chu, W., Forster, R.R., 2020. Direct observation of winter meltwater drainage from the Greenland Ice Sheet. Geophys. Res. Lett. 47 (9) e2019GL086521.
Porter, C., Morin, P., Howat, I., Noh, M.-J., Bates, B., Peterman, K., Keesey, S., Schlenk, M., Gardiner, J., Tomko, K., Willis, M., Kelleher, C., Cloutier, M., Husby, E., Foga, S.,

Nakamura, H., Platson, M., Wethington, M., Jr., Williamson, C., Bauer, G., Enos, J., Arnold, G., Kramer, W., Becker, P., Doshi, A., D'Souza, C., Cummens, P., Laurier, F., Bojesen, M., 2018, ArcticDEM, Harvard Dataverse.

Rennermalm, A.K., Smith, L.C., Chu, V.W., Box, J.E., Forster, R.R., Van den Broeke, M.R., Van As, D., Moustafa, S.E., 2013. Evidence of meltwater retention within the Greenland ice sheet. Cryosphere 7 (5), 1433–1445.

Ryan, J.C., Smith, L.C., Van As, D., Cooley, S.W., Cooper, M.G., Pitcher, L.H., Hubbard, A., 2019. Greenland Ice Sheet surface melt amplified by snowline migration and bare ice exposure. Sci. Adv. 5 (3), eaav3738.

Smith, L.C., Isacks, B.L., Forster, R.R., Bloom, A.L., Preuss, I., 1995. Estimation of discharge from braided glacial rivers using ERS 1 synthetic aperture radar: First results. Water Resour. Res. 31 (5), 1325–1329.

Smith, L.C., Isacks, B.L., Bloom, A.L., Murray, A.B., 1996. Estimation of discharge from three braided rivers using synthetic aperture radar satellite imagery: Potential application to ungaged basins. Water Resour. Res. 32 (7), 2021–2034.

Smith, L.C., 1997. Satellite remote sensing of river inundation area, stage, and discharge: a review. Hydrol. Processes 11 (10), 1427–1439.

Smith, L.C., Pavelsky, T.M., 2008. Estimation of river discharge, propagation speed, and hydraulic geometry from space: Lena River, Siberia. Water Resour. Res. 44 (3), W03427.

Smith, L.C., Chu, V.W., Yang, K., Gleason, C.J., Pitcher, L.H., Rennermalm, A.K., Legleiter, C.J., Behar, A.E., Overstreet, B.T., Moustafa, S.E., Tedesco, M., Forster, R. R., LeWinter, A.L., Finnegan, D.C., Sheng, Y., Balog, J., 2015. Efficient meltwater drainage through supraglacial streams and rivers on the southwest Greenland ice sheet. PNAS 112 (4), 1001–1006.

Smith, L.C., Yang, K., Pitcher, L.H., Overstreet, B.T., Chu, V.W., Rennermalm, Å.K., Ryan, J.C., Cooper, M.G., Gleason, C.J., Tedesco, M., Jeyaratnam, J., van As, D., van den Broeke, M.R., van de Berg, W.J., Noël, B., Langen, P.L., Cullather, R.I., Zhao, B., Willis, M.J., Hubbard, A., Box, J.E., Jenner, B.A., Behar, A.E., 2017. Direct measurements of meltwater runoff on the Greenland ice sheet surface. PNAS 114 (50), E10622–E10631.

Smith, L.C., Andrews, L.C., Pitcher, L.H., Overstreet, B.T., Rennermalm, A.K., Cooper, M. G., Cooley, S.W., Ryan, J.C., Miège, C., Kershner, C., Simpson, C.E., 2021. Supraglacial River Forcing of Subglacial Water Storage and Diurnal Ice Sheet Motion. Geophys. Res. Lett. 48 (7) e2020GL091418.

Sundal, A.V., Shepherd, A., Nienow, P., Hanna, E., Palmer, S., Huybrechts, P., 2009. Evolution of supra-glacial lakes across the Greenland Ice Sheet. Remote Sens. Environ. 113 (10), 2164–2171.

Trusel, L.D., Das, S.B., Osman, M.B., Evans, M.J., Smith, B.E., Fettweis, X., McConnell, J. R., Noël, B.P.Y., van den Broeke, M.R., 2018. Nonlinear rise in Greenland runoff in response to post-industrial Arctic warming. Nature 564 (7734), 104–108.

van As, D., Hubbard, A.L., Hasholt, B., Mikkelsen, A.B., van den Broeke, M.R., Fausto, R. S., 2012. Large surface meltwater discharge from the Kangerlussuaq sector of the Greenland ice sheet during the record-warm year 2010 explained by detailed energy balance observations. Cryosphere 6 (1), 199–209.

van As, D., Bech Mikkelsen, A., Holtegaard Nielsen, M., Box, J.E., Claesson Liljedahl, L., Lindbäck, K., Pitcher, L., Hasholt, B., 2017. Hypsometric amplification and routing moderation of Greenland ice sheet meltwater release. Cryosphere 11 (3), 1371–1386.

van den Broeke, M., Bamber, J., Ettema, J., Rignot, E., Schrama, E., van de Berg, W.J., van Meijgaard, E., Velicogna, I., Wouters, B., 2009. Partitioning recent Greenland mass loss. Science 326 (5955), 984–986.

Vernon, C.L., Bamber, J.L., Box, J.E., van den Broeke, M.R., Fettweis, X., Hanna, E., Huybrechts, P., 2013. Surface mass balance model intercomparison for the Greenland ice sheet. Cryosphere 7 (2), 599–614.

Wright, L.D., 1977. Sediment transport and deposition at river mouths: a synthesis. Geol. Soc. Am. Bull. 88 (6), 857–868. https://doi.org/10.1130/0016-7606(1977)88<857:STADAR>2.0.CO;2.

Yang, K., Li, M., Liu, Y., Cheng, L., Huang, Q., Chen, Y., 2015. River detection in remotely sensed imagery using Gabor filtering and path opening. Remote Sens. 7 (7), 8779–8802.

Yang, K., Smith, L.C., 2016. Internally drained catchments dominate supraglacial hydrology of the southwest Greenland Ice Sheet. J. Geophys. Res.: Earth Surf. 121 (10), 1891–1910.

Yang, K., Smith, L.C., Chu, V.W., Pitcher, L.H., Gleason, C.J., Rennermalm, A.K., Li, M., 2016. Fluvial morphometry of supraglacial river networks on the southwest Greenland Ice Sheet. GISci. Remote Sens. 53 (4), 459–482.

Yang, K., Smith, L.C., Fettweis, X., Gleason, C.J., Lu, Y., Li, M., 2019a. Surface meltwater runoff on the Greenland ice sheet estimated from remotely sensed supraglacial lake infilling rate. Remote Sens. Environ. 234, 111459. https://doi.org/10.1016/j.rse.2019.111459.

Yang, K., Smith, L.C., Sole, A., Livingstone, S.J., Cheng, X., Chen, Z., Li, M., 2019b. Supraglacial rivers on the northwest Greenland Ice Sheet, Devon Ice Cap, and Barnes Ice Cap mapped using Sentinel-2 imagery. Int. J. Appl. Earth Obs. Geoinf. 78, 1–13.

Yang, K., Smith, L., van As, D., Pitcher, L., Cooper, M., Li, M., 2021. Seasonal evolution of supraglacial lakes and rivers on the southwestern Greenland Ice Sheet. J. Glaciol. 67 (264), 592–602.

Zuo, Z., Oerlemans, J., 1996. Modelling albedo and specific balance of the Greenland ice sheet: calculations for the Søndre Strømfjord transect. J. Glaciol. 42 (141), 305–317.